



# HHS Public Access

Author manuscript

*Nanomedicine*. Author manuscript; available in PMC 2021 February 01.

Published in final edited form as:

*Nanomedicine*. 2020 February ; 24: 102138. doi:10.1016/j.nano.2019.102138.

## Photomagnetic Prussian blue nanocubes: synthesis, characterization, and biomedical applications

Diego S. Dumani<sup>1,2,†</sup>, Jason R. Cook<sup>3,4,†</sup>, Kelsey P. Kubelick<sup>1,†</sup>, Jeffrey J. Luci<sup>4,5</sup>, Stanislav Y. Emelianov<sup>1,2,\*</sup>

<sup>1</sup>Wallace H. Coulter Department of Biomedical Engineering, Georgia Institute of Technology and Emory University School of Medicine, Atlanta, GA 30332

<sup>2</sup>School of Electrical and Computer Engineering, Georgia Institute of Technology, Atlanta, GA 30332

<sup>3</sup>NanoHybrids, Inc., Austin, TX 78744

<sup>4</sup>Department of Biomedical Engineering, The University of Texas at Austin, TX 78712

<sup>5</sup>Department of Neuroscience and Imaging Research Center, The University of Texas at Austin, Austin, TX 78712

### Abstract

Nanoparticles play an important role in biomedicine. We have developed a method for size-controlled synthesis of photomagnetic Prussian blue nanocubes (PBNCs) using superparamagnetic iron oxide nanoparticles (SPIONs) as precursors. The developed PBNCs have magnetic and optical properties desired in many biomedical diagnostic and therapeutic applications. Specifically, the size-tunable photomagnetic PBNCs exhibit high magnetic saturation, strong optical absorption with a peak at approximately 700 nm, and superior photostability. Our studies demonstrate that PBNCs can be used as MRI and photoacoustic imaging contrast agents *in vivo*. We also showed the utility of PBNCs for labeling and magnetic manipulation of cells. Dual magnetic and optical properties, together with excellent biocompatibility, render PBNCs an attractive contrast agent for both diagnostic and therapeutic applications. The use of SPIONs as precursors for PBNCs provides flexibility and allows researchers to design theranostic agents according to required particle size, optical, and magnetic properties.

### Graphical Abstract

---

\*Corresponding author: stas@gatech.edu.

Author contributions: D.S.D., J.R.C., and K.P.K. contributed equally to this work.

†Equal contribution

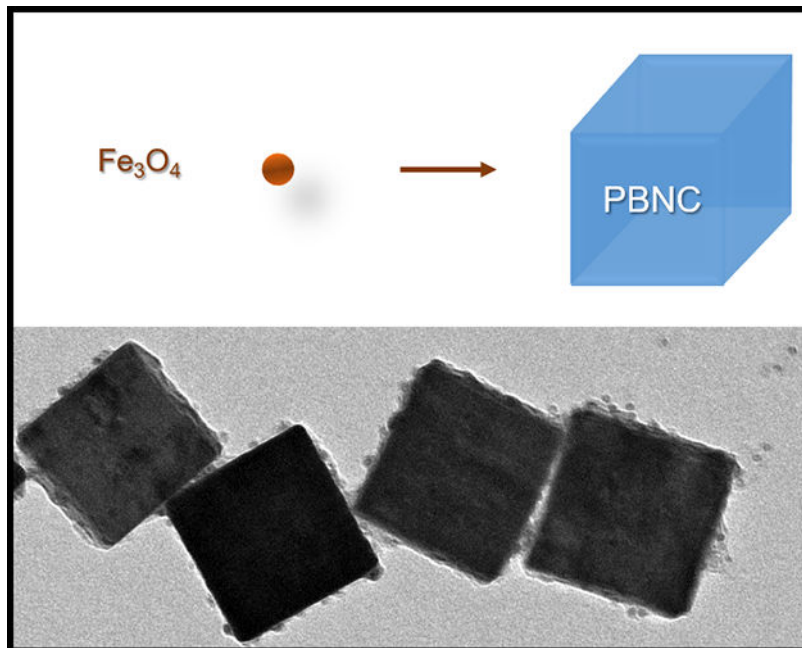
**Publisher's Disclaimer:** This is a PDF file of an unedited manuscript that has been accepted for publication. As a service to our customers we are providing this early version of the manuscript. The manuscript will undergo copyediting, typesetting, and review of the resulting proof before it is published in its final form. Please note that during the production process errors may be discovered which could affect the content, and all legal disclaimers that apply to the journal pertain.

Notes: The authors declare no conflict of interest

Appendix A. Supplementary data

Supplementary data for this article can be found online at [http://dx.doi.org/10.1007/\\*\\*](http://dx.doi.org/10.1007/**).

A method for the synthesis of photomagnetic Prussian blue nanoparticles is presented. Unlike other synthesis schemes, Prussian blue nanocubes are herein synthesized using iron oxide nanoparticles, which allows for tunable size control and enhanced magnetism. Various biomedical applications are explored including MRI, photoacoustic imaging, and magnetic manipulation for cell screening and delivery.



### Keywords

Prussian blue; nanoparticles; size control; magnetic nanoparticle; imaging; photomagnetic

### Background

Nanomaterials have become increasingly used to augment diagnostic and therapeutic capabilities in numerous biomedical and clinically-relevant applications[1–5]. Extensive research has been performed to explore biocompatible nanostructures having optical and magnetic properties suitable for current diagnostic and therapeutic modalities. To date, designing multifunctional theranostic agents of appropriate size, shape, and surface characteristics remains a constant challenge. While no single agent is ideal for all applications and stages of patient care, access to safe, versatile nanomaterials could give clinicians the flexibility needed to design more comprehensive theranostic schemes.

Among many solid nanoparticles, Prussian blue is of interest due in part to its excellent biocompatibility. Prussian blue is approved by the U.S. Food and Drug Administration (FDA), under the brand name Radiogardase®, for treatment of patients with contamination of cesium and/or thallium. However, this clinical indication has nothing to do with Prussian blue's most defining characteristic.

Prussian blue's vibrant blue appearance stems from a very strong optical absorption of red light. Because photon absorption occurs in the tissue optical window (650 – 1300 nm)[6], several preclinical investigations have been performed to assess the feasibility of Prussian blue nanoparticles (PBNPs) as a contrast agent in photoacoustic imaging[7–12] and to enhance heating in photothermal therapy[13–15]. In addition to its visible appearance, Prussian blue is more than 45% iron by mass, endowing it with magnetic properties that have been studied in MRI[13,15,16]. The intrinsic optical and magnetic properties of Prussian blue have also progressed to explorations in multimodal theranostics[8,9,13,15]. However, PBNPs have not been developed and studied to their full potential. Particularly, conventional synthesis methods are prone to variability, resulting in PBNPs of different sizes and properties.

Many PBNP synthesis methods reported in the literature utilize aqueous solutions of iron salts or iron complexes[13–19]. Recent research has led to new synthesis methods which use superparamagnetic iron oxide nanoparticles (SPIONs) composed of  $\text{Fe}_3\text{O}_4$  to create spherical core-shell  $\text{Fe}_3\text{O}_4$ @PBNPs. Reports show these spherical core-shell structures have a diameter of ~15 – 20 nm. In addition to photothermal therapy and magnetic resonance imaging,  $\text{Fe}_3\text{O}_4$ @PBNPs were found to have a unique property – magnetic guidance, due to superparamagnetic nature of the  $\text{Fe}_3\text{O}_4$  core[13,17]. However, synthesis of PBNPs using SPIONs can be greatly expanded. Specifically, we demonstrate that commercially available SPIONs with different diameters can be used to control the size of the resulting PBNPs which is extremely useful for several reasons.

Nanoparticle size is crucial for efficient delivery of therapeutics to target organs. For instance, size is an important factor to predict localization of intravenously-injected nanoparticles. Nanoparticles smaller than 5 nm in size rapidly undergo renal clearance upon intravenous administration[20]. Nanoparticles between 50 – 100 nm are retained in the liver due to spacing of vascular fenestrations and endothelial gaps[21]. Nanoparticles between 200 – 500 nm are retained in the spleen according to the size of the interendothelial cell slits[21]. Large particles in the 2 – 5  $\mu\text{m}$  range have been shown to accumulate in the lungs[21]. Tumors can exhibit a range of fenestrations from 380 – 780 nm[22], which leads to their enhanced permeability and retention (EPR). Nanoparticles in the range of 30 – 100 nm in diameter have exhibited good penetration in a highly permeable tumor, however, in a poorly permeable human pancreatic adenocarcinoma, only nanoparticles smaller than 50 nm in diameter showed accumulation[21].

Based on these examples, smaller particles can be useful when rapid clearance and enhanced permeation are required. In other applications, such as magnetic delivery of nanoparticle-labeled cells, larger constructs that exhibit a stronger response to external fields may be desired. From an imaging perspective, PBNP size and shape may impact magnetic and optical properties to manipulate contrast, as seen in other nanoconstructs.

Clearly the ability to tune the size of PBNPs is critical to enable a variety of applications and to allow researchers to customize PBNPs to meet specific diagnostic and therapeutic needs. With other nanomaterials, such as gold nanorods, use has rapidly advanced by developing new methods to reliably synthesize size-controlled nanoparticles for various

applications[23–26]. For PBNPs, similar opportunities, ranging from particle synthesis to new applications, exist [21,22] if reliable manipulation of PBNP morphology is possible. Therefore, there is a need for development of PBNP synthesis methods to control their size, especially if SPIONs are used as building blocks because of their commercial availability and uniform synthesis according to good manufacturing practices.

We present a facile pseudo-seed-mediated growth method for the synthesis of photomagnetic Prussian blue nanoparticles using  $\text{Fe}_3\text{O}_4$  nanoparticles as the iron source. Various sizes of Prussian blue nanocubes (PBNCs) were produced using SPION precursors with different diameters. The  $\text{Fe}_3\text{O}_4$  SPIONs supply iron to ferrocyanide molecules, which assemble into PBNCs. Thus, the resulting PBNC size is directly related to the size of the  $\text{Fe}_3\text{O}_4$  nanoparticle. In addition to developing a method for PBNC size-control using SPION precursors, our synthesis method produced cubic particles rather than spherical PBNPs. The cubic shape may cause an improvement in imaging and therapeutic efficiency compared with spherical nanoparticles[27–29]. Lastly, we demonstrated various potential applications of our PBNCs as multimodal, multifunctional agents. Although other reports have demonstrated use of PBNPs in other biomedical applications, given our unique synthesis method utility of our PBNCs was unknown. The magnetic and optical properties of our PBNCs proved useful for applications including MRI, photoacoustic imaging, and magnetic manipulation of PBNC-labeled cells, including image-guided magnetic trapping.

## Methods

### Synthesis of PBNCs.

Prussian blue nanocubes were synthesized using SPIONs as localized Fe sources in a pseudo seed-mediated growth mechanism. Size control of the PBNCs was determined by the size of the SPIONs used in the synthesis. The source and synthesis of SPION precursors is described in the Supplementary Data. Stock solutions of the reactant (potassium hexacyanoferrate (II) trihydrate ( $\text{K}_4\text{Fe}(\text{CN})_6 \cdot 3\text{H}_2\text{O}$ ) (5 w/w %)) and catalyst (HCl in DIUF (1.85 v/v %)) for PBNC synthesis were prepared in advance. Under vigorous stirring, dextran-coated SPIONs (60 mg) were added to DIUF water (150 ml). The solution was briefly stirred to ensure full dispersion of SPIONs. Then, the reactant stock solution (7.5 ml) was added. The reaction was stirred for 1 minute, and the catalyst solution (2.5 ml) was added. The reaction was stirred for at least 1 hour. The solution became a deep blue color as the PBNCs formed. When necessary, further stabilization was performed as described in the Supplementary Data. Following synthesis, the UV-Vis absorbance spectrum of PBNCs was measured using a Synergy HT Microplate Reader (BioTek).

### Transmission electron microscopy.

Transmission electron microscopy (TEM) (Hitachi HT7700 TEM) was used to characterize the PBNCs, 5 nm diameter SPIONs, and 10 nm diameter SPIONs. Small SPIONs (3 nm) were imaged using a FEI Tecnai G2 F20 X-Twin TEM. Sample preparation is described in the Supplementary Data. Size distribution of all particles was analyzed using ImageJ software (Figure S1). The size standard deviation of each population was divided by its respective mean to obtain the particle size coefficient of variation (Figure S2).

**Elemental analysis.**

Elemental analysis via energy-dispersive X-ray spectroscopy was performed using a Hitachi HD-2700 STEM/SEM. Carbon-formvar grids were prepared as described for TEM in Supplementary Data. Because of the grid composition, carbon was not included as part of the elemental analysis.

**SQUID magnetometry.**

The magnetic properties of PBNCs and SPIONS were studied using a superconducting quantum interference device (SQUID) magnetometer (MPMS-5S, Quantum Design). Sample preparation is described in the Supplementary Data.

**MRI relaxometry.**

MRI contrast properties were measured using a 3T MRI scanner (MAGNETOM Skyra 3T MRI, Siemens) and a low-field 0.5T NMR spectrometer (Maran Ultra 23, Resonance, Oxford, UK). Sample preparation and data analysis are described in the Supplementary Data.

**Photostability.**

To test photostability, PBNCs were irradiated using a 5-ns pulsed laser, following a previously described procedure[30]. A 1 mm diameter glass tube served as the sample holder and was filled with either PBNCs, PEGylated gold nanorods (PEG-AuNR), or silica-coated gold nanorods (SiO<sub>2</sub>-AuNR), with absorption peaks between 680 and 700 nm. 20-nm PBNCs were used to match the absorption peaks of the AuNR. All samples had an optical density  $OD = 1 \text{ cm}^{-1}$ . The samples were exposed to 900 laser pulses at various fluences ranging from 5 to 28  $\text{mJ}\cdot\text{cm}^{-2}$  (irradiation and acquisition details are described in the Supplementary Data). For each fluence, and for each different sample, the tube was irradiated with 900 laser pulses and the PA signal was recorded (Figure S6). The absorption spectrum stability was further studied by irradiating a 96-well plate containing samples of PBNCs or PEG-AuNR with 900 laser pulses of fluences from 3 to 20  $\text{mJ}\cdot\text{cm}^{-2}$ . After the irradiation experiment, UV-Vis measurements were taken to analyze any spectrum variations due to laser exposure. Results were normalized based on absorbance before irradiation.

**MRI imaging.**

A 7T preclinical MRI system (Bruker PharmaScan) was used for tissue-mimicking phantom imaging experiments. PBNCs of three sizes were imaged in a tissue-mimicking gelatin phantom, described in the Supplementary Data. A *T2 RARE* sequence with  $TR = 2500 \text{ ms}$  and  $TE = 35 \text{ ms}$  was used to enhance  $T_2$ -weighted contrast.

**Ultrasound and photoacoustic imaging.**

A Vevo LAZR (VisualSonics, Canada) imaging system, incorporating ultrasound and photoacoustic (US/PA) modalities was used for phantom, in vitro, and in vivo US/PA imaging experiments. US/PA images were acquired using 20 and 40 MHz (LZ250 and LZ550) center frequency, 256-element transducers. Laser irradiation (tunable 680–970 nm

wavelength, 7 ns pulse, 20 pulses per second) was delivered by an optical fiber integrated into the imaging transducer.

### **In vivo animal studies.**

All animal procedures were approved by the Institutional Animal Care and Use Committee (IACUC) at the Georgia Institute of Technology. A female nude mouse (Nu/Nu, Charles River) was anesthetized and injected subcutaneously in the abdomen with two boli consisting of PBS in 50 v/v % Matrigel matrix (Corning), and 20-nm dextran-coated PBNCs,  $OD = 40 \text{ cm}^{-1}$ , in 50 v/v % Matrigel. MRI and US/PA images were acquired subsequently. A 7T preclinical MRI system (Bruker PharmaScan) was used to acquire in vivo images. The anesthetized mouse was placed in a cylindrical holder to be inserted in the imaging coil. A built-in *Flash* imaging sequence modified with  $TR = 500 \text{ ms}$ , and  $TE = 3.3 \text{ ms}$  was utilized to increase  $T_2^*$ -weighting and identify the PBNCs.

US/PA images were acquired as described above, using a Vevo LAZR with a 20 MHz LZ250 transducer. The mouse was placed on a heating pad and imaged under anesthesia. Multiwavelength imaging was performed with wavelengths from 700 nm to 970 nm in steps of 2 nm. Following imaging experiments the mice were euthanized by  $\text{CO}_2$  asphyxiation. The photoacoustic spectra at the injection sites is shown in Figure S7a (see Supplementary Data). The normalized spectra (Figure S7b) distinguished different photoabsorbers (i.e., PBNC vs hemoglobin).

### **Cell phantom imaging.**

Macrophages, Human epithelial breast cancer cells (MDA-MB-231), and Human adipose-derived mesenchymal stem cells (MSC) were cultured as described in the Supplementary Data. Cells were incubated with PBNCs for 24 hours and washed prior to phantom preparation. PBNC-labeled cells were imaged in a tissue-mimicking gelatin phantom, described in the Supplementary Data. US/PA images of the gelatin phantom were acquired for wavelengths between 680 and 970 nm at an imaging frame rate of 5 Hz.

### **Magnetic Delivery and US/PA imaging.**

Magnetic trapping experiments were set up by running a 0.062" inner diameter x 0.095" outer diameter, clear silicone tube (HelixMark®) through a 10×10×10 cm clear plastic box. Two ring neodymium magnets (NR0082–45NM, CMS Magnetics, Garland, TX) were fixed at opposite ends of the box to apply a magnetic field along the tube and initially magnetize the particles. The tube passed through the center of each ring magnet. Several small neodymium brick magnets (N42, K&J Magnetics, Inc., Pipersville, PA) were fixed below the center of the tube to produce a gradient for trapping. Cells labeled with 20-nm PBNCs, concentrated at  $5,000 \text{ cells}\cdot\text{ml}^{-1}$ , were circulated through the tube at a flow rate of  $0.5 \text{ ml}\cdot\text{min}^{-1}$ . US/PA images were collected along the length of the tube using  $\lambda = 700 \text{ nm}$  by connecting a 20 MHz (LZ250) transducer to a 3D translation motor.

## Results

### Size control

To demonstrate the size control of the synthesized PBNCs, we used 3, 5, and 10 nm diameter Fe<sub>3</sub>O<sub>4</sub> nanoparticles as iron sources to produce PBNCs measuring 20, 40, and 170 nm edge length, respectively. Indeed, TEM images show that PBNC size varied depending on the SPION precursor size (Figure 1). PBNCs were well dispersed in all cases (Figure 1a–c). Small PBNCs with approximately 20 nm edge length resulted from 3 nm diameter SPION precursors. Medium (40 nm edge length) PBNCs resulted from 5 nm diameter SPION precursors, and large (170 nm edge length) PBNCs resulted from 10 nm SPIONs. Thus, the size of resulting PBNCs was dependent on the diameter of SPION precursors (Figure 1g). All sample sizes approximated a single-population normal distribution (Supplementary Data, Figure S1).

Measurements suggest that polydispersity of the precursor had an effect in the size distribution of resulting PBNCs. Due to challenges of size-separating extremely small SPIONs synthesized in house, a wider range of particle diameters was present in the 3-nm SPION sample compared with the 5-nm and 10-nm SPIONs. The 3-nm SPIONs were more polydisperse based on the coefficient of variation and hence led to more polydisperse 20 nm PBNCs (Supplementary Data, Figure S2). This further demonstrates the ability for size control of PBNCs.

Elemental analysis of PBNCs using energy-dispersive X-ray spectroscopy showed a homogeneous distribution of iron, potassium, nitrogen, and oxygen, the reaction reagents, confirming that the reaction did not consist of a surface coating but rather a synthesis of a homogenous nanocube. The SPIONs are thus homogeneously distributed inside the cubes that were formed (Supplementary Data, Figure S3). Prussian blue has a molecular formula of C<sub>18</sub>Fe<sub>7</sub>N<sub>18</sub> and produces a relatively large face centered crystal structure (Fm3m space group)[31]. The iron atoms within the crystals are in an octahedral configuration, which helps strengthen the compound and enables large single crystalline formation. Therefore, the natural configuration for this crystalline structure is cubic.

The magnetic and optical properties of PBNCs were characterized, and nanoparticles were tested for feasibility in various applications.

### Magnetic and optical properties

PBNCs had an optical absorption peak at approximately 700 nm, which is within the near-infrared (NIR) optical window where tissue allows deepest light penetration. The optical absorption spectrum of the 20-nm, 40-nm, and 170-nm PBNCs were comparable (Figure 2a). Slight NIR shift of peak extinction coefficient was observed – this is likely due to increased optical scattering from larger PBNCs.

The magnetism of small 20-nm PBNCs and their 3-nm SPION precursors was analyzed using a superconducting quantum interference device (SQUID) as shown in Figure 2b. PBNCs exhibited superparamagnetism with a magnetic saturation of 104.0 emu/g (nanoparticle mass) or 228.6 emu/g (iron mass). SPIONs exhibited a magnetic saturation of

20.5 emu/g (nanoparticle mass) or 28.3 emu/g (iron mass). This corresponds to a 5-fold and 8-fold increase in magnetization, when comparing based on nanoparticle mass and iron mass, respectively. These values also exceed the magnetic saturation of 66 emu/g reported for 20 nm SPIONs[32]. Interestingly, previous studies showing modification of magnetite nanoparticles usually imply a reduction of their magnetization, compared with pure SPIONs[13,33–36]. Furthermore, previous studies generated spherical nanoconstructs rather than cubical. The shape has been shown to have an effect on the magnetic properties of cubic vs. spherical nanoparticles, and a cubic shape could potentially increase the efficiency for magnetic manipulation and hyperthermia[27–29].

Similarly, superparamagnetism of nanomaterials is dependent on their size, shape, and crystal structure[37,38]. While magnetization increases with particle size, there is a size limit below which particles remain superparamagnetic (i.e. superparamagnetic limit). For  $\text{Fe}_3\text{O}_4$ , it has been reported that particles exhibit superparamagnetism when below 20 nm[38–40]. The results presented in this study show that the superparamagnetic limit of PBNCs is at least as high as that of  $\text{Fe}_3\text{O}_4$ . This feature can be valuable whenever larger magnetization and/or particle sizes are needed, while preserving superparamagnetic properties. Having higher magnetic susceptibility than the clinically used SPION counterparts, together with their high NIR absorption, makes the developed PBNCs attractive multimodal, multifunctional agents.

To test feasibility of our PBNCs as MRI contrast agents, relaxometry studies were performed using a 3 T clinical MRI scanner (MAGNETOM Skyra 3T MRI, Siemens), and a 0.5 T NMR spectrometer (Maran Ultra 23, Resonance). To calculate the molecular weights,  $\text{Fe}_3\text{O}_4$  and  $\text{C}_{18}\text{Fe}_7\text{N}_{18}$  were assumed for SPIONs and PBNCs, respectively. The measured transverse relaxivity values are found in Table 1. Detailed procedures are found in the Supplementary Data.

The longitudinal ( $r_1$ ) and transverse ( $r_2$ ) relaxivities of 20-nm PBNCs at 3T were  $0.375 \text{ mM}^{-1}\text{s}^{-1}$  and  $13.66 \text{ mM}^{-1}\text{s}^{-1}$ , respectively. The obtained values exceed those previously reported using conventional PBNC synthesis methods under 1.5 T and 7 T field strengths[41]. In addition to the different field strength, this could be attributed to water exchange-related differences affecting the relaxivity and fluctuations in the local magnetic field, known as inner sphere and outer sphere effects[42–44]. Additionally, the PBNC likely contains SPIONs embedded within the cubic lattice, causing an underestimation of the PBNC mass. However, the analysis of these differences is outside the scope of the current study.

Additional relaxometry studies were performed using the 0.5 T NMR, to compare the SPION precursors and the resulting PBNCs. Transverse relaxivity was  $1.11 \text{ mM}^{-1}\text{s}^{-1}$  for 3-nm SPIONs. After synthesis, 20-nm PBNCs had a  $10.05 \text{ mM}^{-1}\text{s}^{-1}$  transverse relaxivity, showing a 9-fold increase over their precursor. However, the size-matched 20-nm SPIONs had a transverse relaxivity of  $920 \text{ mM}^{-1}\text{s}^{-1}$ . Thus, for the same particle size, SPIONs still provide a better relaxivity than their PBNC counterparts. The large 170-nm PBNCs had a transverse relaxivity of  $402.4 \text{ mM}^{-1}\text{s}^{-1}$ , a 40-fold increase over the smaller 20-nm PBNCs, showing the scalable magnetic properties with increasing PBNC size. The  $r_2/r_1$  ratio, an

indicator of an effective  $T_2$  contrast agent, ranged from 1.02 to 16.43 for 20-nm to 170-nm PBNCs at 0.5 T.

While commercial MRI agents offer better molar relaxivity than PBNCs[45–48], this could be overcome by using higher doses due to the low toxicity of Prussian blue[41]. Indeed, the recommended daily oral dose for Radiogardase® in adults is 9 grams up to 20 grams, corresponding to 10.5 up to 23.3 mmol, with no overdose described. Although a recommended dosage has not been established for IV use of Prussian blue, it could potentially be higher than those of commercial agents, such as gadolinium-based Gadavist® (100  $\mu\text{mol/kg}$ ,  $r_1 = 5.0 \text{ mM}^{-1}\text{s}^{-1}$ ,  $r_2 = 7.1 \text{ mM}^{-1}\text{s}^{-1}$ ) and SPION-based Sinerem®/Combix® (45  $\mu\text{mol Fe/kg}$ ,  $r_1 = 6.58 \text{ mM}^{-1}\text{s}^{-1}$ ,  $r_2 = 127.8 \text{ mM}^{-1}\text{s}^{-1}$ ).

### Photoacoustic stability

While there are various reports on photoacoustic (PA) applications of PBNCs, their photothermal stability under pulsed laser irradiation, which has important implications for long-term therapeutic and imaging purposes, has not been fully characterized. We tested the stability of our PBNCs using various pulsed laser energies below and above American National Standards Institute (ANSI) safety limits[49]. Unlike the more commonly used gold nanorods (degraded at  $8.5 \text{ mJ}\cdot\text{cm}^{-2}$ ) and silica-coated gold nanorods (degraded at  $13 \text{ mJ}\cdot\text{cm}^{-2}$ ), no degradation in the PA signal was observed up to  $28 \text{ mJ}\cdot\text{cm}^{-2}$  (Figure 3a). Within this range, photoacoustic signal from PBNCs scaled linearly with fluence, demonstrating enhanced robustness as opposed to gold nanorods, which showed substantial photodegradation with all fluences greater than  $5 \text{ mJ}\cdot\text{cm}^{-2}$  (Figure 3a,c). Furthermore, the absorbance spectrum of PBNCs also remained stable after irradiation with 900 laser pulses up to  $20 \text{ mJ}\cdot\text{cm}^{-2}$  (Figure 3b).

In addition to benefits of magnetism and biocompatibility, the isotropic, non-plasmonic nature of PBNCs means they are less prone to degradation than anisotropic plasmonic particles, such as nanorods. For imaging in the NIR, PBNCs would outperform many commonly used contrast agents including nanoparticles and dyes. PBNCs remain stable during repeated laser irradiation, enabling longer term imaging and therapeutic applications. This, together with their high molar absorption in the NIR[50], demonstrates PBNCs' suitability as photoacoustic agents.

### Combined MRI and photoacoustic imaging

To assess the feasibility of PBNCs as multimodal contrast agents, the nanoparticles were imaged in a tissue-mimicking gelatin phantom prior to animal experiments. In the phantom, PBNCs of all sizes generated high contrast in  $T_2$ -weighted MR images (Figure 4a). US waves are not sensitive to small, nanometer size PBNCs thus the US images do not exhibit contrast. However, PA imaging obtained with 740-nm laser irradiation confirmed stability and photoacoustic contrast of PBNCs (Figure 4b,c). Additionally, the photoacoustic spectra matched the expected NIR absorption for all particle sizes based on UV-Vis measurements (Figure 4d).

Animal imaging experiments validated the in vivo utility of PBNCs. First, a bolus of 20-nm PBNCs in Matrigel was injected subcutaneously on one side of a mouse abdomen. A control bolus containing PBS in Matrigel was injected on the opposite side.

MRI of the injected area confirmed contrast enhancement by PBNCs. A modified *Flash* sequence was performed to enhance  $T_2^*$  contrast and identify the PBNCs. The injection site with PBNCs appeared dark due to the influence of PBNCs on  $T_2^*$  relaxation (Figure 5a). Conversely, the control injection did not show any contrast enhancement. In the case of regions of interest having low concentrations of PBNCs or tissues with dark background signals, a multi-echo sequence using incrementally increasing TE times could better indicate presence of PBNCs by assessing rates of decay and differences in  $T_2$  relaxation times.

Following MRI, US/PA imaging was performed on the same mouse. The injected area showed high contrast on the PBNC-loaded bolus and low signal on the control bolus (Figure 5b). The signal of PBNC injection at 700 nm was approximately 5-fold higher than the control injection. Additionally, the absorption spectra from multiwavelength PA imaging confirmed presence of PBNC, while the control bolus only displayed low endogenous signals from hemoglobin (Supplementary Data, Figure S7). Non-negligible skin PA signals were also present, indicating that multiwavelength spectroscopic analysis may be needed to distinguish small concentrations of PBNCs from background contrast.

In a clinical setting, these imaging modalities could be exploited synergistically to provide full-body agent location using MRI, together with local analysis with high spatial and temporal resolution using US/PA imaging.

### Image-guided magnetic trapping

A new potential application of PBNCs is image-guided magnetic trapping of cells. We performed in vitro experiments to verify successful cell labeling and feasibility of photoacoustic imaging. PBNCs were used to label cancer cells and were imaged in a tissue-mimicking gelatin phantom. Inclusions of 20-nm PBNCs in deionized ultra-filtered water (DIUF) or cell culture media were also included to evaluate differences in PA signal upon cellular uptake.

PBNCs in DIUF did not produce any ultrasound (US) contrast because of their small particle size. The same sample generated a strong PA signal; however, because the particles remained homogeneously distributed in water, the signal was largely confined to the edges of the inclusion (Figure 6a<sub>i</sub>).

Cell culture media caused local agglomerations of PBNCs, making the particles more visible in ultrasound images compared to the samples in DIUF, because larger particle aggregates produced detectable ultrasound scattering. These localized agglomerations also introduced inhomogeneities that allowed PA signal to be more visible throughout the inclusion rather than limited to the edges (Figure 6a<sub>ii</sub>).

Cancer cells labeled with 20-nm PBNCs were detectable with both ultrasound and PA imaging (Figure 6a<sub>iii</sub>). PA signal appeared throughout the inclusion because cell uptake further increased local particle agglomeration. Mesenchymal stem cells were also

successfully labeled by PBNCs, generating comparable images (Figure 6a<sub>iv</sub>). The photoacoustic spectra of the labeled cells (Figure 6b) matched the expected result based on the UV-vis spectra and PA spectra of PBNCs in DI water.

Imaging and cell labeling experiments further confirmed PBNCs' performance as stable photoacoustic contrast agents when using our new synthesis method. In addition, PBNC absorption was not affected by cell uptake, as indicated by the measured PA spectra.

Due to the superparamagnetism of PBNCs, PBNC-labeled cells can be manipulated using external magnetic fields. Conversely, cells labeled with citrated gold nanospheres (AuNP), i.e. non-magnetic, do not respond to external magnets (Figure 6c). We demonstrated the multifunctional utility of the PBNCs in a mock cell screening apparatus. Cells labeled with 20-nm PBNCs were circulated through a silicone tube with a magnetic trap. Two ring magnets produced a homogeneous field to initially magnetize the labeled cells, as previously shown in literature[51]. A bar magnet on the side of the tube applied a gradient to trap cells. Ultrasound and photoacoustic images were acquired along the length of the tube and overlaid to show where cells collected (Figure 6d insert). The ultrasound and photoacoustic signals of the tube were represented by gray scale and red scale, respectively. A spike in the PA signal was confined to the magnet location and corresponded to a 5-fold increase in the PA signal (Figure 6d).

By using an external magnetic field, PBNCs can be directed to a desired location for diagnostic and therapeutic purposes. The potential applications of this feature include circulating tumor cell screening, magnetic targeting, and magnetic delivery/manipulation of therapeutic agents. Controlled nanoparticle movement can also be used for image guidance, such as magnetomotive US/PA imaging. Magnetomotive imaging allows sensitive detection of particles by assessing changes in speckle patterns due to particle movement upon application of a pulsed magnetic field.

## Discussion

In addition to the results shown, PBNCs possess capabilities for numerous additional applications. Prussian blue's high affinity to heavy metals may be exploited beyond heavy metal poisoning treatment, its current clinical use. This attribute could allow tagging of PBNCs with compounds such as barium sulfate to enable X-ray imaging contrast[52]. Besides magnetic manipulation and magnetomotive imaging techniques, PBNC's magnetic properties could enhance magnetic hyperthermia using alternating magnetic fields, potentially improving therapeutic penetration depth[29,53], with the possibility to be combined with photothermal therapy to augment heating capability[54].

The ability to consistently vary the size of the PBNCs according to SPION precursors' diameter further adds to imaging and therapeutic possibilities. Studies have shown that particle size can impact the effectiveness of Prussian blue in treatment of heavy metal poisoning[55,56]. Moreover, it has been shown that the size and shape of single-domain particles can affect their magnetic properties, which may influence their behavior in magnetic manipulation and heating applications[32,57–60].

Our reaction scheme takes advantage of the decades of previous work to optimize Fe<sub>3</sub>O<sub>4</sub> nanoparticles. Currently, there are numerous commercial sources of Fe<sub>3</sub>O<sub>4</sub> nanoparticles that provide monodisperse colloidal aqueous solutions with diameters ranging from 5 nm to greater than 50 nm. Furthermore, numerous forms of Fe<sub>3</sub>O<sub>4</sub> nanoparticles have been FDA approved for various applications, so rigorous protocols for large batch production and thorough physicochemical characterization have been optimized for the FDA required current Good Manufacturing Practices (cGMP)[61]. This reduces the costs and will allow for quicker clinical translation of Prussian blue nanoparticle-based applications.

While SPIONs are ubiquitous in applications involving nanoparticle-magnetic field interactions, such as MRI, magnetically-guided drug delivery, and magnetomotive imaging, the developed PBNCs offer the enhanced benefit of NIR absorption while maintaining strong magnetization properties. The strong optical absorption alone makes PBNCs a great option for applications including photoacoustic imaging, optical microscopy, and photothermal therapy.

In conclusion, we presented a facile method for size-controlled synthesis of photomagnetic PBNCs using SPIONs, obtained commercially or synthesized in-house, as precursors. We demonstrated that the size of the PBNCs can be controlled by the size of the SPIONs. Because highly monodisperse SPIONs are available commercially, this synthesis gives researchers a facile method to produce PBNCs with excellent size control. The photomagnetic PBNCs possess the attractive optical properties previously shown with conventional syntheses and enhance the magnetic properties of PBNCs. We confirmed the in vitro and in vivo utility of PBNCs as imaging agents for MRI and photoacoustic imaging. Additionally, we took advantage of magnetic properties to show potential for novel diagnostic and therapeutic applications such as circulating tumor cell screening and magnetically-guided cell delivery. The results demonstrate the potential of PBNCs in optical and magnetic based applications. Overall, our novel synthesis method represents a toolbox for researchers to easily tailor PBNCs by tuning and optimizing the desired nanoparticle size according to the requirements of each particular application, helping to expand the biomedical uses of PBNCs.

## Supplementary Material

Refer to Web version on PubMed Central for supplementary material.

## Acknowledgments

The authors would like to acknowledge Dr. Eric Drew of the Georgia Institute of Technology for his help with SQUID measurements, Dr. Johannes Leisen, Dr. Jisha V.S, and Dr. In-Cheol Sun for insightful discussions, and Dr. Justin Harris from NanoHybrids for assistance with TEM of small SPIONs.

This work was performed in part at the Georgia Tech Institute for Electronics and Nanotechnology, a member of the National Nanotechnology Coordinated Infrastructure, which is supported by the National Science Foundation (Grant ECCS-1542174).

Funding: This work was supported in part the Breast Cancer Research Foundation [grant number BCRF-19-043]; and National Institutes of Health [grant numbers EB008101, CA158598, CA149740].

## References

1. Zhang L, Gu F, Chan J, Wang A, Langer R, and Farokhzad O, Nanoparticles in medicine: therapeutic applications and developments. *Clinical Pharmacology & Therapeutics*, 2008 83(5): p. 761–769. [PubMed: 17957183]
2. Bobo D, Robinson KJ, Islam J, Thurecht KJ, and Corrie SR, Nanoparticle-based medicines: a review of FDA-approved materials and clinical trials to date. *Pharmaceutical Research*, 2016 33(10): p. 2373–2387. [PubMed: 27299311]
3. Eifler AC and Thaxton CS, Nanoparticle therapeutics: FDA approval, clinical trials, regulatory pathways, and case study, in *Biomedical Nanotechnology*. 2011, Springer p. 325–338.
4. Stafford S, Serrano Garcia R, and Gun'ko YK, Multimodal Magnetic-Plasmonic Nanoparticles for Biomedical Applications. *Applied Sciences*, 2018 8(1): p. 97.
5. Santiesteban DY, Kubelick K, Dhada KS, Dumani D, Suggs L, and Emelianov S, Monitoring/Imaging and Regenerative Agents for Enhancing Tissue Engineering Characterization and Therapies. *Annals of Biomedical Engineering*, 2016 44(3): p. 750–772. [PubMed: 26692081]
6. Smith AM, Mancini MC, and Nie S, Bioimaging: second window for in vivo imaging. *Nature Nanotechnology*, 2009 4(11): p. 710–711.
7. Liang X, Deng Z, Jing L, Li X, et al., Prussian blue nanoparticles operate as a contrast agent for enhanced photoacoustic imaging. *Chemical Communications*, 2013 49(94): p. 11029–11031. [PubMed: 23884328]
8. Cheng L, Gong H, Zhu W, Liu J, et al., PEGylated Prussian blue nanocubes as a theranostic agent for simultaneous cancer imaging and photothermal therapy. *Biomaterials*, 2014 35(37): p. 9844–9852. [PubMed: 25239041]
9. Jing L, Liang X, Deng Z, Feng S, et al., Prussian blue coated gold nanoparticles for simultaneous photoacoustic/CT bimodal imaging and photothermal ablation of cancer. *Biomaterials*, 2014 35(22): p. 5814–5821. [PubMed: 24746962]
10. Reguera E, Marín E, Calderón A, and Rodríguez-Hernández J, Photo-induced charge transfer in Prussian blue analogues as detected by photoacoustic spectroscopy. *Spectrochimica Acta Part A: Molecular and Biomolecular Spectroscopy*, 2007 68(1): p. 191–197.
11. Ozeki T, Matsumoto K, and Hikime S, Photoacoustic spectra of prussian blue and photochemical reaction of ferric ferricyanide. *Analytical Chemistry*, 1984 56(14): p. 2819–2822.
12. Kim T, Lemaster JE, Chen F, Li J, and Jokerst JV, Photoacoustic imaging of human mesenchymal stem cells labeled with Prussian Blue–poly (l-lysine) nanocomplexes. *ACS nano*, 2017 11(9): p. 9022–9032. [PubMed: 28759195]
13. Fu G, Liu W, Li Y, Jin Y, et al., Magnetic Prussian blue nanoparticles for targeted photothermal therapy under magnetic resonance imaging guidance. *Bioconjugate Chemistry*, 2014 25(9): p. 1655–1663. [PubMed: 25109612]
14. Hoffman HA, Chakrabarti L, Dumont MF, Sandler AD, and Fernandes R, Prussian blue nanoparticles for laser-induced photothermal therapy of tumors. *RSC Advances*, 2014 4(56): p. 29729–29734.
15. Li Z, Zeng Y, Zhang D, Wu M, et al., Glypican-3 antibody functionalized Prussian blue nanoparticles for targeted MR imaging and photothermal therapy of hepatocellular carcinoma. *Journal of Materials Chemistry B*, 2014 2(23): p. 3686–3696. [PubMed: 32263805]
16. Shokouhimehr M, Soehnlén ES, Khitrin A, Basu S, and Huang SD, Biocompatible Prussian blue nanoparticles: Preparation, stability, cytotoxicity, and potential use as an MRI contrast agent. *Inorganic Chemistry Communications*, 2010 13(1): p. 58–61.
17. Xue P, Bao J, Zhang L, Xu Z, et al., Functional magnetic Prussian blue nanoparticles for enhanced gene transfection and photothermal ablation of tumor cells. *Journal of Materials Chemistry B*, 2016 4(27): p. 4717–4725. [PubMed: 32263244]
18. Zhang X-Q, Gong S-W, Zhang Y, Yang T, Wang C-Y, and Gu N, Prussian blue modified iron oxide magnetic nanoparticles and their high peroxidase-like activity. *Journal of Materials Chemistry*, 2010 20(24): p. 5110–5116.

19. Thammawong C, Opaprakasit P, Tangboriboonrat P, and Sreearunothai P, Prussian blue-coated magnetic nanoparticles for removal of cesium from contaminated environment. *Journal of nanoparticle research*, 2013 15(6): p. 1689.
20. Choi HS, Liu W, Misra P, Tanaka E, et al., Renal clearance of quantum dots. *Nature Biotechnology*, 2007 25(10): p. 1165–1170.
21. Blanco E, Shen H, and Ferrari M, Principles of nanoparticle design for overcoming biological barriers to drug delivery. *Nature Biotechnology*, 2015 33(9): p. 941–951.
22. Hobbs SK, Monsky WL, Yuan F, Roberts WG, et al., Regulation of transport pathways in tumor vessels: role of tumor type and microenvironment. *Proceedings of the National Academy of Sciences*, 1998 95(8): p. 4607–4612.
23. Nikoobakht B and El-Sayed MA, Preparation and growth mechanism of gold nanorods (NRs) using seed-mediated growth method. *Chemistry of Materials*, 2003 15(10): p. 1957–1962.
24. Kim F, Song JH, and Yang P, Photochemical synthesis of gold nanorods. *Journal of the American Chemical Society*, 2002 124(48): p. 14316–14317. [PubMed: 12452700]
25. Huang X, Neretina S, and El-Sayed MA, Gold nanorods: from synthesis and properties to biological and biomedical applications. *Advanced materials*, 2009 21(48): p. 4880–4910. [PubMed: 25378252]
26. Chen Y-S, Zhao Y, Yoon SJ, Gambhir SS, and Emelianov S, Miniature gold nanorods for photoacoustic molecular imaging in the second near-infrared optical window. *Nature nanotechnology*, 2019: p. 1.
27. Salazar-Alvarez G, Qin J, Sepelak V, Bergmann I, et al., Cubic versus spherical magnetic nanoparticles: the role of surface anisotropy. *Journal of the American Chemical Society*, 2008 130(40): p. 13234–13239. [PubMed: 18783216]
28. Noh S.-h., Na W, Jang J.-t., Lee J-H, et al., Nanoscale magnetism control via surface and exchange anisotropy for optimized ferrimagnetic hysteresis. *Nano letters*, 2012 12(7): p. 3716–3721. [PubMed: 22720795]
29. Martinez-Boubeta C, Simeonidis K, Makridis A, Angelakeris M, et al., Learning from nature to improve the heat generation of iron-oxide nanoparticles for magnetic hyperthermia applications. *Scientific Reports*, 2013 3: p. 1652. [PubMed: 23576006]
30. Chen Y-S, Frey W, Kim S, Homan K, et al., Enhanced thermal stability of silica-coated gold nanorods for photoacoustic imaging and image-guided therapy. *Optics Express*, 2010 18(9): p. 8867–8878. [PubMed: 20588732]
31. Rauwel P and Rauwel E, Towards the Extraction of Radioactive Cesium-137 from Water via Graphene/CNT and Nanostructured Prussian Blue Hybrid Nanocomposites: A Review. *Nanomaterials*, 2019 9(5): p. 682.
32. Sutens B, Swusten T, Zhong K, Jochum JK, et al., Tunability of size and magnetic moment of iron oxide nanoparticles synthesized by forced hydrolysis. *Materials*, 2016 9(7): p. 554.
33. Alvarez-Paino M, Marcelo G, Munoz-Bonilla A, Rodriguez-Hernandez J, and Fernandez-Garcia M, Surface modification of magnetite hybrid particles with carbohydrates and gold nanoparticles via “click” chemistry. *Polymer Chemistry*, 2013 4(4): p. 986–995.
34. Kim YS, Lee HJ, Govindaiah P, Son W, et al., Preparation of Fe<sub>3</sub>O<sub>4</sub>-embedded poly (styrene)/poly (thiophene) core/shell nanoparticles and their hydrogel patterns for sensor applications. *Materials*, 2014 7(1): p. 195–205. [PubMed: 28788450]
35. Rittikulsittichai S, Singhana B, Bryan WW, Sarangi S, et al., Preparation, characterization, and utilization of multi-functional magnetic-fluorescent composites for bio-imaging and magnetic hyperthermia therapy. *RSC Advances*, 2013 3(21): p. 7838–7849.
36. Zhang H, Zhang Q, Zhang B, and Guo F, Preparation of magnetic composite microspheres by surfactant free controlled radical polymerization: Preparation and characteristics. *Journal of Magnetism and Magnetic Materials*, 2009 321(23): p. 3921–3925.
37. Leslie-Pelecky DL and Rieke RD, Magnetic properties of nanostructured materials. *Chemistry of Materials*, 1996 8(8): p. 1770–1783.
38. Li Q, Kartikowati CW, Horie S, Ogi T, Iwaki T, and Okuyama K, Correlation between particle size/domain structure and magnetic properties of highly crystalline Fe<sub>3</sub>O<sub>4</sub> nanoparticles. *Scientific Reports*, 2017 7(1): p. 9894. [PubMed: 28855564]

39. Jeun M, Lee S, Kyeong Kang J, Tomitaka A, et al., Physical limits of pure superparamagnetic Fe<sub>3</sub>O<sub>4</sub> nanoparticles for a local hyperthermia agent in nanomedicine. *Applied Physics Letters*, 2012 100(9): p. 092406.
40. Kim D, Lee N, Park M, Kim BH, An K, and Hyeon T, Synthesis of uniform ferrimagnetic magnetite nanocubes. *Journal of the American Chemical Society*, 2008 131(2): p. 454–455.
41. Shokouhimehr M, Soehnlén ES, Hao J, Griswold M, et al., Dual purpose Prussian blue nanoparticles for cellular imaging and drug delivery: a new generation of T<sub>1</sub>-weighted MRI contrast and small molecule delivery agents. *Journal of Materials Chemistry*, 2010 20(25): p. 5251–5259.
42. Koenig SH and Brown III RD, Field-cycling relaxometry of protein solutions and tissue: implications for MRI. *Progress in Nuclear Magnetic Resonance Spectroscopy*, 1990 22(6): p. 487–567.
43. Kowalewski J, Nordenskiöld L, Benetis N, and Westlund P-O, Theory of nuclear spin relaxation in paramagnetic systems in solution. *Progress in Nuclear Magnetic Resonance Spectroscopy*, 1985 17: p. 141–185.
44. Lauffer RB, Paramagnetic metal complexes as water proton relaxation agents for NMR imaging: theory and design. *Chemical Reviews*, 1987 87(5): p. 901–927.
45. Rohrer M, Bauer H, Mintorovitch J, Requardt M, and Weinmann H-J, Comparison of magnetic properties of MRI contrast media solutions at different magnetic field strengths. *Investigative Radiology*, 2005 40(11): p. 715–724. [PubMed: 16230904]
46. León-Rodríguez D, Luis M, Martins AF, Pinho MC, Rofsky NM, and Sherry AD, Basic MR relaxation mechanisms and contrast agent design. *Journal of Magnetic Resonance Imaging*, 2015 42(3): p. 545–565. [PubMed: 25975847]
47. Simon GH, Bauer J, Saborovski O, Fu Y, et al., T<sub>1</sub> and T<sub>2</sub> relaxivity of intracellular and extracellular USPIO at 1.5 T and 3T clinical MR scanning. *European Radiology*, 2006 16(3): p. 738–745. [PubMed: 16308692]
48. Jung CW and Jacobs P, Physical and chemical properties of superparamagnetic iron oxide MR contrast agents: ferumoxides, ferumoxtran, ferumoxsil. *Magnetic Resonance Imaging*, 1995 13(5): p. 661–674. [PubMed: 8569441]
49. American National Standards Institute. United States of America Standards, I., American national standard for the safe use of lasers. 2014.
50. Fu G, Liu W, Feng S, and Yue X, Prussian blue nanoparticles operate as a new generation of photothermal ablation agents for cancer therapy. *Chemical Communications*, 2012 48(94): p. 11567–11569. [PubMed: 23090583]
51. Wei C.w., Xia J, Pelivanov I, Jia C, et al., Magnetomotive photoacoustic imaging: in vitro studies of magnetic trapping with simultaneous photoacoustic detection of rare circulating tumor cells. *Journal of Biophotonics*, 2013 6(6–7): p. 513–522. [PubMed: 23420803]
52. Meagher MJ, Leone B, Turnbull TL, Ross RD, Zhang Z, and Roeder RK, Dextran-encapsulated barium sulfate nanoparticles prepared for aqueous dispersion as an X-ray contrast agent. *Journal of Nanoparticle Research*, 2013 15(12): p. 2146.
53. Goya GF, Asín L, and Ibarra MR, Cell death induced by AC magnetic fields and magnetic nanoparticles: current state and perspectives. *International Journal of Hyperthermia*, 2013 29(8): p. 810–818. [PubMed: 24131333]
54. Espinosa A, Di Corato R, Kolosnjaj-Tabi J, Flaud P, Pellegrino T, and Wilhelm C, Duality of iron oxide nanoparticles in cancer therapy: amplification of heating efficiency by magnetic hyperthermia and photothermal bimodal treatment. *ACS Nano*, 2016 10(2): p. 2436–2446. [PubMed: 26766814]
55. Kravzov J, Rios C, Altagracia M, Monroy-Noyola A, and Lopez F, Relationship between physicochemical properties of Prussian blue and its efficacy as antidote against thallium poisoning. *Journal of Applied Toxicology*, 1993 13(3): p. 213–216. [PubMed: 8326092]
56. Faustino PJ, Yang Y, Progar JJ, Brownell CR, et al., Quantitative determination of cesium binding to ferric hexacyanoferrate: Prussian blue. *Journal of Pharmaceutical and Biomedical Analysis*, 2008 47(1): p. 114–125. [PubMed: 18242038]

57. Guardia P, Di Corato R, Lartigue L, Wilhelm C, et al., Water-soluble iron oxide nanocubes with high values of specific absorption rate for cancer cell hyperthermia treatment. *ACS Nano*, 2012 6(4): p. 3080–3091. [PubMed: 22494015]
58. Fortin J-P, Wilhelm C, Servais J, Ménager C, Bacri J-C, and Gazeau F, Size-sorted anionic iron oxide nanomagnets as colloidal mediators for magnetic hyperthermia. *Journal of the American Chemical Society*, 2007 129(9): p. 2628–2635. [PubMed: 17266310]
59. Usov N and Grebenshchikov YB, Influence of surface anisotropy on magnetization distribution in a single-domain particle. *Journal of Applied Physics*, 2008 104(4): p. 043903.
60. Schäffer AF, Sukhov A, and Berakdar J, Size-dependent frequency bands in the ferromagnetic resonance of a Fe-nanocube. *Journal of Magnetism and Magnetic Materials*, 2017 438: p. 70–75.
61. FDA, Guidance for Industry and FDA Staff: Current Good Manufacturing Practice Requirements for Combination Products. 2015, U.S. Food and Drug Administration: Silver Spring, MD.

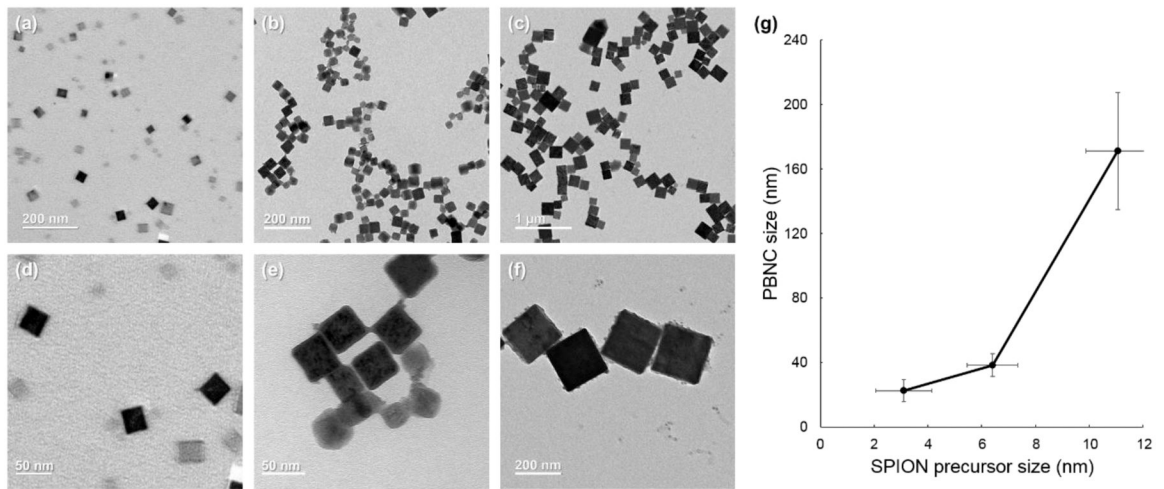


**Figure 1.**

TEM images of size-controlled PBNCs. (a) 20-nm PBNCs synthesized from 3-nm SPION precursors. (b) 40-nm PBNCs synthesized from 5-nm SPION precursors. (c) 170-nm PBNCs synthesized from 10-nm SPION precursors. (d-f) Images at increased magnification for 20-nm, 40-nm, and 170-nm PBNCs, respectively. (g) Scatter plot showing relationship between SPION precursors and resulting PBNC size.

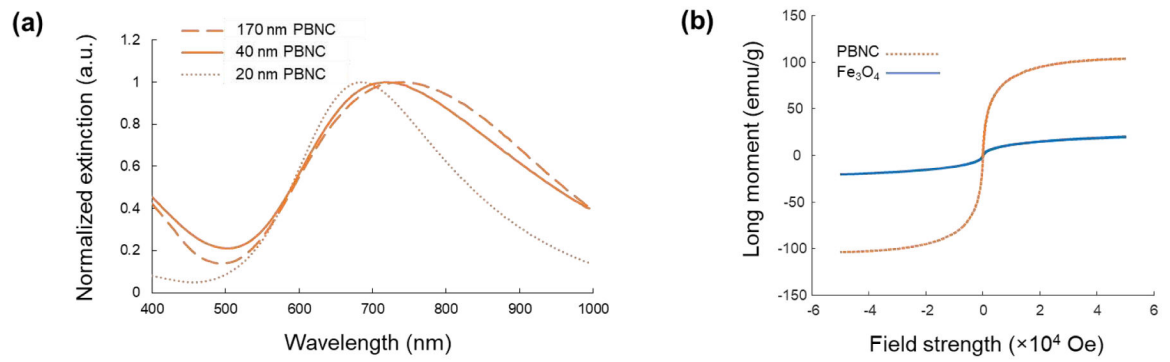


**Figure 2.** Magnetic and optical properties of PBNCs. (a) UV-Vis spectrometry shows 20-nm, 40-nm, and 170-nm PBNCs' NIR absorbance peaks at 685 nm, 720 nm, and 740 nm, respectively. (b) Magnetic moment curves show a 5-fold increase in magnetization for 20-nm PBNCs compared to  $\text{Fe}_3\text{O}_4$  based on nanoparticle mass.

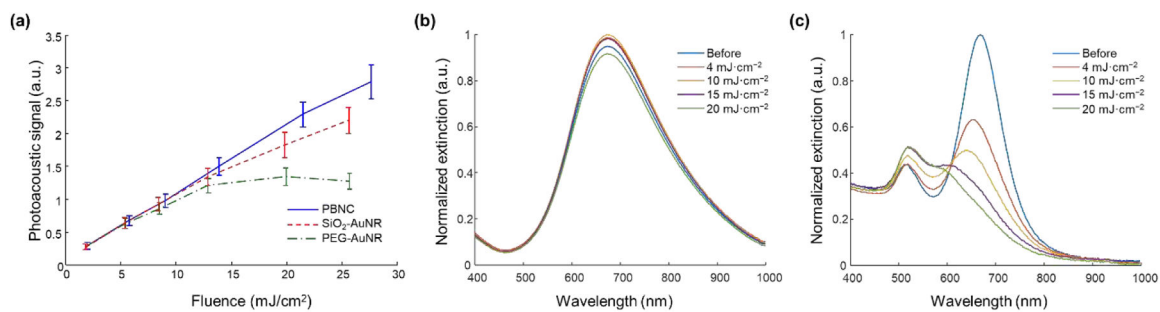


**Figure 3.** Photothermal stability. (a) Photoacoustic signal from PBNCs, PEGylated gold nanorods (PEG-AuNR) and silica-coated gold nanorods (SiO<sub>2</sub>-AuNR) at different fluences. PBNCs remained stable and conserve linearity with fluence when exposed to 900 laser pulses beyond 25 mJ·cm<sup>-2</sup>. AuNR showed degradation beyond 5 mJ·cm<sup>-2</sup> (b) The absorbance spectrum of PBNCs remained stable after 900 laser pulses up to 20 mJ·cm<sup>-2</sup>. (c) Gold nanorods' spectra showed degradation for all energies between 4 and 20 mJ·cm<sup>-2</sup>.

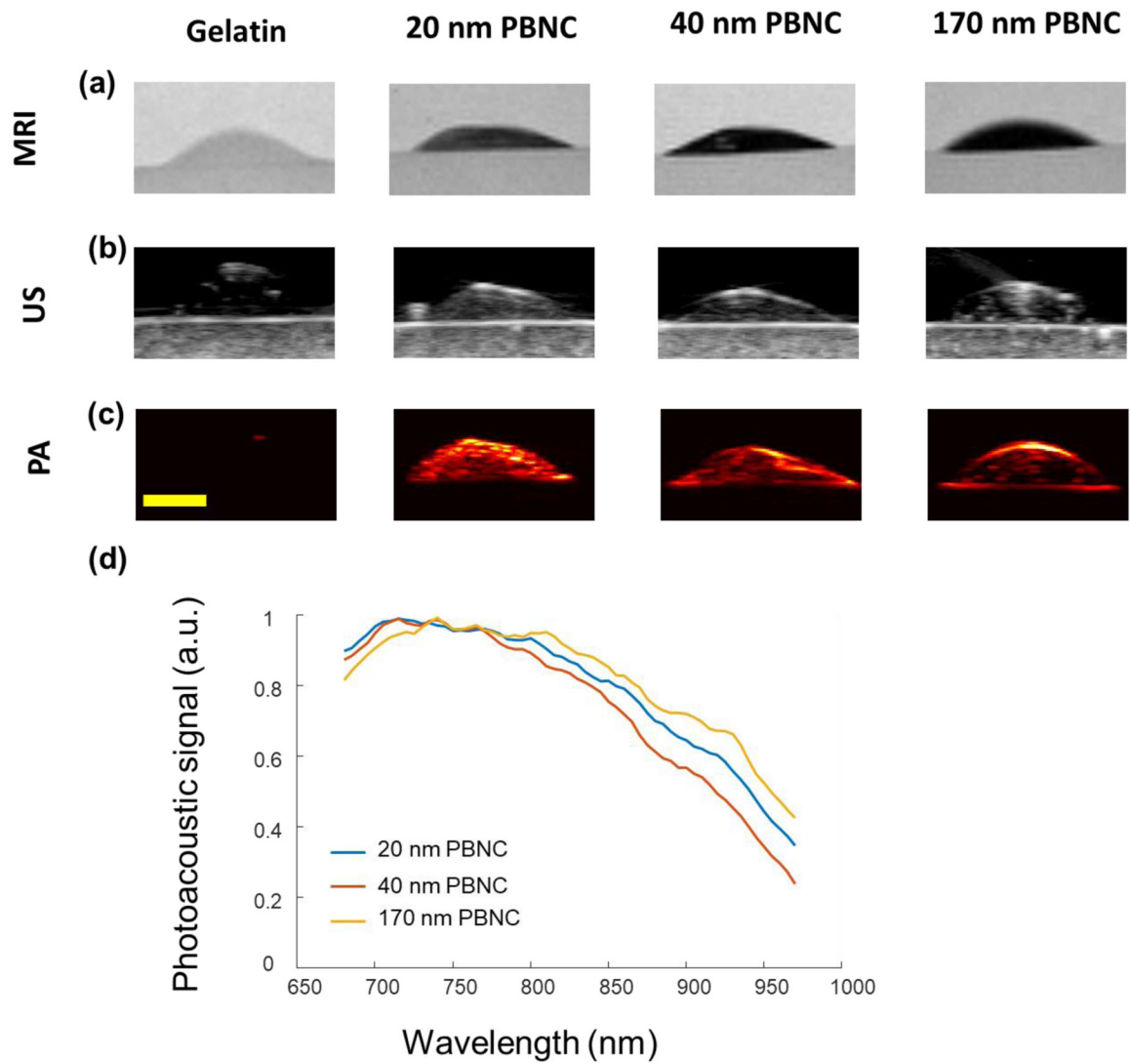


**Figure 4.** (a) T<sub>2</sub>-weighted MRI, (b) ultrasound (US), and (c) photoacoustic imaging (PA) at 740 nm, of PBNCs in a tissue-mimicking gelatin phantom. Scale bar = 2 mm. (d) The photoacoustic spectra match the expected NIR absorption for all particle sizes.

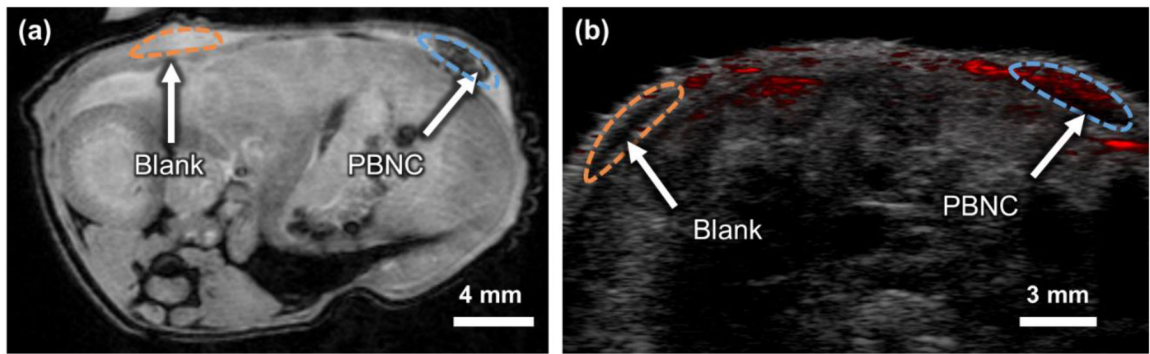


**Figure 5.**

In vivo imaging of axial cross section of a mouse abdomen following subcutaneous injection of PBS in Matrigel (Blank, orange contour) and Prussian blue nanocubes in Matrigel (PBNC, blue contour). (a) MRI image with a *Flash* sequence with TR = 500 ms and TE = 3.3 ms. (b) Ultrasound and photoacoustic image at 700 nm.

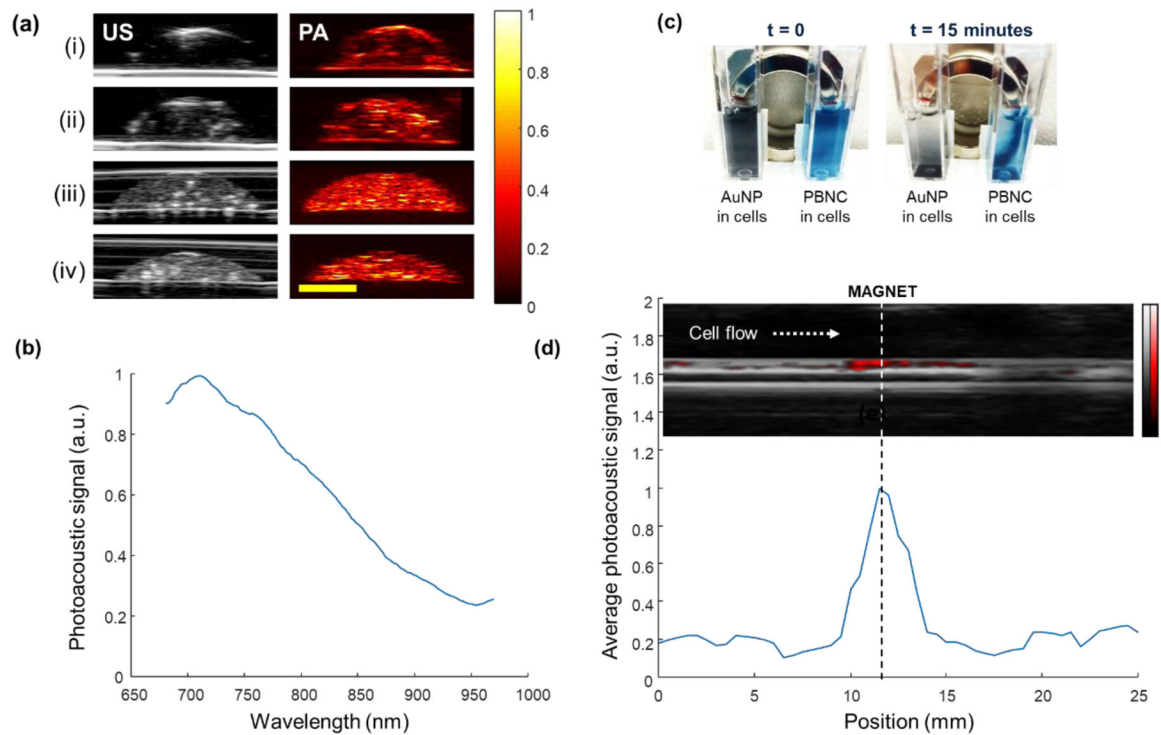


**Figure 6.** Image-guided magnetic trapping of cells labeled with 20-nm PBNCs. Tissue-mimicking phantom studies (a) confirmed PBNC-labeled cells produced a PA signal. (a) Ultrasound (US, gray scale) and photoacoustic (PA, color map) imaging of 20-nm PBNCs in (i) DIUF, (ii) cell culture media, (iii) PBNC-labeled cancer cells, and (iv) PBNC-labeled mesenchymal stem cells. (b) Photoacoustic spectrum of cancer cells labeled with 20-nm PBNCs. Scale bar = 2 mm. (c) PBNC-labeled cells can be manipulated using an external magnet, as opposed to the AuNP-labeled cells (control). (d) Inset: ultrasound (gray scale) and photoacoustic (color scale) image of capillary tube with PBNC-labeled cells trapped at the bar magnet, indicated by the dashed line. The integrated PA signal along the tube length shows a 5-fold PA signal increase at the gradient magnet position.

**Table 1.**

Transverse molar relaxivity of SPIONs and PBNCs

Magnetic field	Nanoparticle size and type	Transverse relaxivity $r_2$ [ $\text{mM}^{-1}\text{s}^{-1}$ ]
0.5 T	3-nm SPION	1.11
0.5 T	10-nm SPION	316.0
0.5 T	20-nm SPION	920.8
0.5 T	20-nm PBNC	10.05
0.5 T	40-nm PBNC	34.0
0.5 T	170-nm PBNC	402.4

Author Manuscript

Author Manuscript

Author Manuscript

Author Manuscript